DE GRUYTER Nanotechnology Reviews 2021; 10: 1912–1925

Research Article

Poonam Dwivedi*, Indu Jatrana, Azhar U. Khan*, Azmat Ali Khan, Honey Satiya, Masudulla Khan, Il Soo Moon, and Mahboob Alam*

Photoremediation of methylene blue by biosynthesized ZnO/Fe_3O_4 nanocomposites using *Callistemon viminalis* leaves aqueous extract: A comparative study

https://doi.org/10.1515/ntrev-2021-0117
received September 7, 2021; accepted October 26, 2021

Abstract: This article reports a simple, cost-effective, and eco-friendly biosynthesis of ZnO/Fe_3O_4 nanocomposites using *Callistemon viminalis* leaves' water extract. For the first time, we used a green synthetic route *via C. viminalis* leaves' extract to prepare ZnO/Fe_3O_4 nanocomposites (NCs) using zinc acetate and ferric chloride as precursor materials. Fourier transform infrared (FTIR) spectroscopic results revealed polyphenolic compounds mainly phenolic acids present in the plant extract acted as both reducing and stabilizing agents to synthesize ZnO/Fe_3O_4 NCs. Outcomes of XRD and X-ray photoelectron spectroscopy confirmed the formation of ZnO–Fe_3O_4 heterojunction in ZnO/Fe_3O_4 NCs, with crystallite sizes of 45, 35, and 60 nm, respectively, according to Debye–Scherrer's formula. EDX confirmed Zn, Fe, and O in the ZnO/Fe_3O_4 nanocomposite. Scanning electron microscopy and transmission electron microscopy (TEM) analyses revealed the existence of both ZnO and Fe_3O_4 in the NCs with some agglomeration. The thermal stability of NCs was evaluated using thermogravimetric analysis (TGA) and differential thermal analysis (DTA) in a nitrogen atmosphere. In addition, as-prepared ZnO/Fe_3O_4 NCs along with biosynthesized ZnO and Fe_3O_4 (prepared by *C. viminalis* extract) nanoparticles were examined for photodegradation of methylene blue under visible light irradiation for 150 min. The result reveals that the photodegradation efficiency of ZnO/Fe_3O_4 NCs (99.09%) was higher compared to that of monometallic ZnO (84.7%) and Fe_3O_4 (37.1%) nanoparticles.

Keywords: ZnO/Fe_3O_4 nanocomposites, *Callistemon viminalis*, XPS, photodegradation, methylene blue

1 Introduction

Industrialization and urbanization have increased water pollution to a great extent because of the direct disposal of organic and industrial waste into water bodies [1]. Among all, dying industries produce an enormous amount of wastewater containing unused dye along with other chemicals [2]. It reported that the majority of dyes are toxic and nonbiodegradable [3]. Hence, the dye effluent contaminates surface and underground water, which brings out adverse effects on flora and fauna [4,5]. Methylene blue (MB) is the most popular thiazine dye used in textile industries. The prolonged exposure to MB results in harmful effects, such as cyanosis, skin irritation, and gastrointestinal irritation, in living beings [6]. To solve this challenge, many physical and chemical techniques including flocculation–coagulation, surface adsorption, ion-exchange, chemical precipitation, and photocatalytic degradation have been used to remove the dye from waste water [7,8]. Because of the simple experimental procedure and decomposition of organic dye molecules into nontoxic simple

---

*** Corresponding author: Poonam Dwivedi,** Department of Chemistry, School of Basic Sciences, Jaipur National University, Jaipur, 302017, India, e-mail: dwdpoonam@gmail.com
*** Corresponding author: Azhar U. Khan,** Department of Chemistry, School of Life and Basic Sciences, SIILAS Campus, Jaipur National University, Jaipur, 302017, India, e-mail: azhar.u.kh@gmail.com
*** Corresponding author: Mahboob Alam,** Division of Chemistry and Biotechnology, Dongguk University, 123 Dongdae-Ro, Gyeongju, 780-714, Republic of Korea, e-mail: mahboobchem@gmail.com
Indu Jatrana, Honey Satiya: Department of Chemistry, School of Basic Sciences, Jaipur National University, Jaipur, 302017, India
Azmat Ali Khan: Pharmaceutical Biotechnology Laboratory, Department of Pharmaceutical Chemistry, College of Pharmacy, King Saud University, Riyadh, 11451, Saudi Arabia
Masudulla Khan: Botany Section, Women's College, Aligarh Muslim University, Aligarh, U.P. 202002, India
Il Soo Moon: Department of Anatomy, Dongguk University College of Medicine, Gyeongju, 38066, Republic of Korea

products in the presence of semiconductors under proper light irradiation, the photodegradation process proves its superiority over other methods [9,10]. For semiconductor-assisted photocatalytic process, various materials, such as ZnO, CuO, TiO_2, and more, have been widely used as photocatalysts previously [11–13]. Among different semiconductor materials, ZnO is a nontoxic, easily available, and cost-effective material with a bandgap of 3.2 and 60 MeV exciton binding energy [14]. That is why ZnO became the priority to many researchers working in the photocatalytic degradation of dyes using semiconductors. But ZnO semiconductor has a rapid tendency of recombination of photo-induced electron–hole pairs, which makes it difficult to gain the practical demand [15]. To overcome this problem, many metallic or nonmetallic materials, such as CdS, Ag_2O, CuO, and g-C_3N_4, have doped with ZnO and showed improved efficiency toward photodegradation process [16–19].

However, the removal of nanocomposites (NCs) from the treated solution is very tedious and expensive, which is still a challenge. In this concern, magnetite nanoparticles (Fe_3O_4 NPs) play an effective role as they are easily separable from the solution by applying an external magnetic field [20]. Apart from this, doping of metallic NPs with magnetite NPs improves their functionality and recyclability and in turn cost effectiveness of the process [21,22]. Inspired by this, many researchers have synthesized and investigated the results of magnetite NCs [23]. After reviewing the literature, we observed that various approaches, such as sol–gel, hydrothermal synthesis, precipitation, and microemulsion, have been adopted for preparing magnetite composites [24–27]. But many of these methods have certain demerits, such as the use of expensive and hazardous chemicals and the formation of toxic byproducts, which makes it difficult to achieve the requirement of green synthesis. In recent decades, the use of bioproducts (including biomolecules, bacteria, fungi, or plant extracts) for the synthesis of NPs has attracted researchers as well [28]. Metals and metal oxide nanoparticles have also been used as homogeneous or heterogeneous nanocatalysts in various organic syntheses due to the large surface-to-volume ratio of nanoparticles compared to bulk materials [29,30]. This strategy provides a simple, cost-effective, and eco-friendly route for the fabrication of nanomaterials [31]. Although synthesis of ZnO/Fe_3O_4 NCs by different routes has been reported [32,33], a few reports on a green synthesis of ZnO/Fe_3O_4 NCs are available [34,35]. In our present study, we have synthesized ZnO/Fe_3O_4 NCs using *Callistemon viminalis* leaves' extract as a green reducing and stabilizing agent. *C. viminalis* is a small tree that belongs to the family Myrtaceae with a characteristic brushlike flowers. It is a traditional medicine to treat hemorrhoids, gastroenteritis, diarrhea, and skin infection [36–38]. The phytochemical study reported that *C. viminalis* is rich in biomolecules, including viminadiones, quercetin, and betulinic acid, and can act as a green reducing and capping agent during the fabrication of nanomaterials.

After reviewing the literature, we understand that *C. viminalis* leaves' extract-mediated biomimetic synthesis of ZnO/Fe_3O_4 has not been reported till date. In this study, we have attempted to understand the role of biomolecules present in leaves' extract as a reducing and stabilizing agent for the fabrication of ZnO/Fe_3O_4 NCs. The novelty of this study is to show the efficacy of biosynthesized ZnO/Fe_3O_4 NCs as a photocatalyst in contrast to ZnO or Fe_3O_4 NPs for the degradation of MB solution under visible light irradiation.

2 Experimental methodology

2.1 Chemicals

All chemicals applied in this research study, including zinc acetate dihydrate (Thermo Fisher Scientific India Pvt. Ltd.), ferric chloride (Thermo Fisher Scientific India Pvt. Ltd.), sodium hydroxide (Merck Life Science India Pvt. Ltd.), and methylene blue (Merck Life Science India Pvt. Ltd.), were of analytical grade and used as received commercially without further purification. Deionised water was used throughout the experiment wherever required.

2.2 Preparation of *C. viminalis* leaves' extract

Leaves of *C. viminalis* were collected from Jaipur National University campus, India. The collected leaves were thoroughly washed under tap water and finally washed using deionised water. After drying in shade, the leaves were powdered in an electrical grinder. About 25 g of the powdered leaves in 100 mL deionised water was refluxed in a Soxhlet apparatus (Sigma-Aldrich, India) for 2 h at 80°C on a magnetic stirrer. On cooling, the suspension was filtered through Whatmann's filter paper, and the filtrate was collected as leaves' extract and stored in a refrigerator at 2°C for further studies.

2.3 Biosynthesis of ZnO/Fe_3O_4 NCs

The ZnO/Fe_3O_4 NCs were prepared through an eco-friendly green route, and the synthesis procedure is briefly illustrated as follows: 30 mL of *C. viminalis* leaves' extract was added slowly in a round-bottom flask containing 30 mL of zinc acetate solution (0.01 M) under stirring. After 10 min, 0.16 g of ferric chloride in 10 mL deionised water was introduced dropwise into the flask and heated to 60°C, followed by the addition of NaOH (0.1 M) to maintain pH 10. The color of the solution changes from black to blackish brown after 1 h stirring, which indicated the formation of ZnO/Fe_3O_4 NCs. Afterward, the solution was cooled to room temperature, centrifuged, collected in a China dish, washed several times with ethanol to remove unused extract and NaOH, dried in an oven at 80°C, and finally calcined at 300°C before storing for further studies. For comparison, monometallic nanoparticles (ZnO and Fe_3O_4) had also been synthesized using *C. viminalis* leaves' extract. A schematic of aforementioned green synthesis is shown in Figure 1.

2.4 Characterization

FTIR spectral analysis in the range of 4,000–400 cm^{-1} was carried out to investigate the role of *C. viminalis* leaf extract in the fabrication of ZnO, Fe_3O_4, and ZnO/Fe_3O_4 nanoproducts using a PerkinElmer spectrophotometer (MNIT, Jaipur). A powder X-ray diffraction technique was performed to determine the crystallinity and particle size of biosynthesized product by PAN analytical (XPART PRO) diffractometer in the scattering range (2θ) of 20–80° using Cu Kα radiation ($\lambda = 1.5406$ Å). The surface morphology of green synthesized samples was determined by scanning electron microscopy (SEM) using Nova Nano SEM 450 (MNIT, Jaipur) and transmission electron microscopy (TEM) at IIT Roorkee. The elemental composition was investigated using EDX analysis. Chemical states of elements present in ZnO/Fe_3O_4 NCs were analyzed by X-ray photoelectron spectroscopic technique (XPS, PHI 5000 Versa Probe III, IIT Roorkee). The thermal stability of ZnO/Fe_3O_4 sample was recorded in a nitrogen atmosphere at a heating rate of 5°C min^{-1} by TGA/DTA analyzer (EXSTAR TG/DTA 6300, IIT Roorkee).

2.5 Designing of the photocatalytic activity experiment

The photocatalytic efficiency of biosynthesized ZnO, Fe_3O_4, and ZnO/Fe_3O_4 nanomaterials for the degradation of MB dye was evaluated under visible light at pH 7. For the

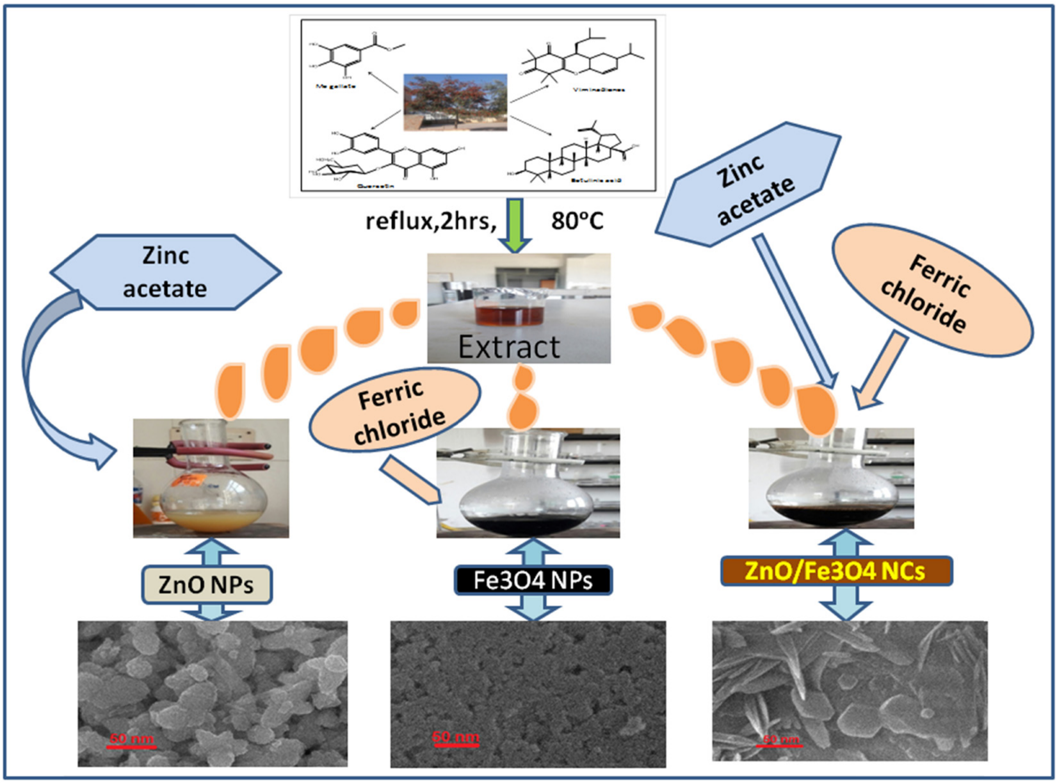

Figure 1: Schematic of green synthesis of ZnO NPs, Fe_3O_4 (NPs), and ZnO/Fe_3O_4 NCs.

photodegradation study, three experimental sets were prepared. Each set comprised seven beakers (100 mL) with 25 mL solution of MB (32 mg L^{-1}) in each. The dose of biosynthesized ZnO, Fe_3O_4, or ZnO/Fe_3O_4 nanoproducts taken was 0.004 g in each beaker. After certain intervals of time (15, 30, 45, 60, 75, 90, and 150 min), one beaker from each set was removed from irradiation, and dye solutions were centrifuged at 8,000 rpm followed by filtration to remove the photocatalyst. MB degradation was examined by measuring the absorbance of the dye solution at $\lambda_{\max} = 665$ nm using a UV-Vis spectrophotometer. The percentage of MB degradation was determined by the following equation:

$$\eta = A_0 - A_t/A_0 \times 100. \qquad (1)$$

In equation (1), η is the degradation percentage and A_0 and A_t are the absorbances of MB dye solution at $t = 0$ and after time t, respectively.

3 Results and discussion

3.1 FTIR analysis

The involvement of biomolecules present in *C. viminalis* leaves' extract, for the fabrication of nanomaterials, was screened by FTIR spectroscopic analysis. Figure 2 depicts the FTIR spectra of *C. viminalis* leaves' extract as well as biosynthesized ZnO, Fe_3O_4, and ZnO/Fe_3O_4 nanomaterials. The FTIR spectrum of *C. viminalis* leaves' extract (Figure 2a) showed some major absorption bands at 3,419, 2921.76, 1718.16, 1451.86, 1368.87, and 1180.95 cm^{-1} were assigned to O–H stretching of phenolic acids and phenols, C–H stretching in CH_3 and CH_2, C=O groups in phenolic acids and flavonoids, C=C stretching of the aromatic ring, and C–H deformation in CH_3 and C–OH stretching in phenolic acids, respectively, as reported in various literature [39–41].

However, after the reduction of metal precursors into their respective metal nanoparticles, a remarkable difference in intensity, position, and shape of absorption peaks had been observed, which showed the participation of biomolecules (present in leaves' extract) in the reduction and capping of nanomaterials. The additional peaks in the spectra of monometallic NPs at 466.53 cm^{-1} (Figure 2(b)) and 612 cm^{-1} (Figure 2(c)) were allocated to Zn–O and Fe–O stretching vibrations, respectively, confirming the formation of ZnO and Fe_3O_4 NPs [42]. Moreover, shifting in absorption peak values of Zn–O (452.93 cm^{-1}) and Fe–O (591.63 cm^{-1}) towards lower wave numbers in ZnO/Fe_3O_4 (Figure 2(d)) indicated the formation of bimetallic nanocomposite. Furthermore, shrinkage/shifting of peaks corresponding to C=O, C=C, and C–OH groups (1718.16, 1451.86, and 1180.95 cm^{-1}) in the spectra of nanoproducts

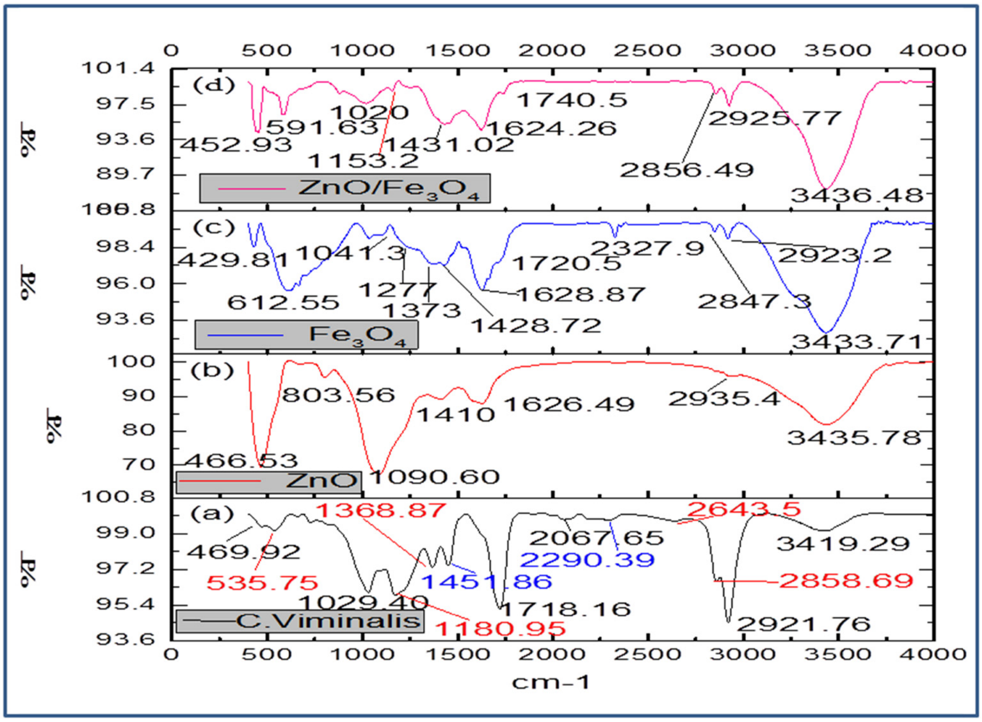

Figure 2: FTIR spectra of (a) *C. viminalis* leaf extract, (b) ZnO, (c) Fe_3O_4, and (d) ZnO/Fe_3O_4 NCs.

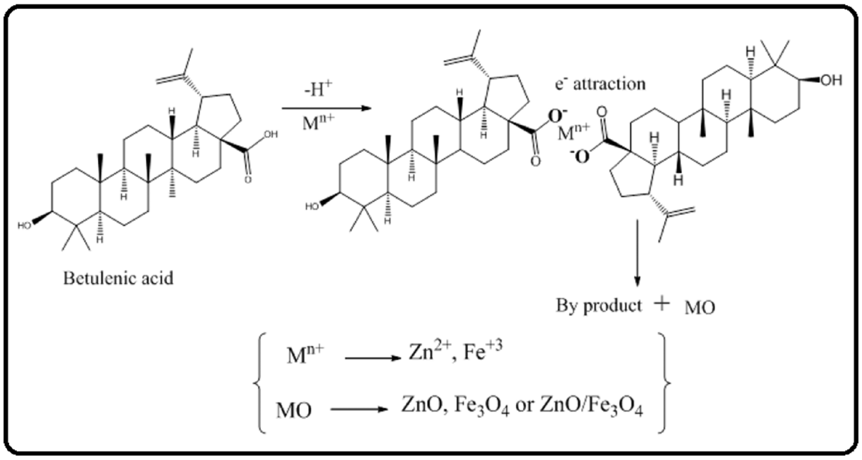

Scheme 1: Proposed mechanism for the biosynthesis of ZnO, Fe_3O_4, and ZnO/Fe_3O_4 NCs.

suggests that polyphenolic compounds mainly phenolic acids are responsible for the bioreduction of metal ions and capping of as-prepared nanoproducts.

3.1.1 Mechanism of biosynthesis

On the basis of FTIR results, a possible mechanism for the *C. viminalis* leaves' extract-mediated synthesis of ZnO, Fe_3O_4, and ZnO/Fe_3O_4 has been proposed.

In short, betulinic acid present in leaves' extract undergoes oxidation according to the free radical mechanism, that is, betulinic acid to dehydro betulinic acid (Scheme 1). Zn^{+2}/Fe^{+3} ions (present in solution) form complex with dehydro betulinic acid *via* transfer of electrons from anionic dehydro betulinic acid to metal ions. On calcination, the resulting complex is converted into respective metal oxide nanoparticles because of the capping effect of biomolecules [43].

3.2 XRD analysis

The phase and crystal structure of biosynthesized ZnO, Fe_3O_4, and ZnO/Fe_3O_4 nanomaterials were examined by powder X-ray diffraction analysis. Figure 3 depicts the

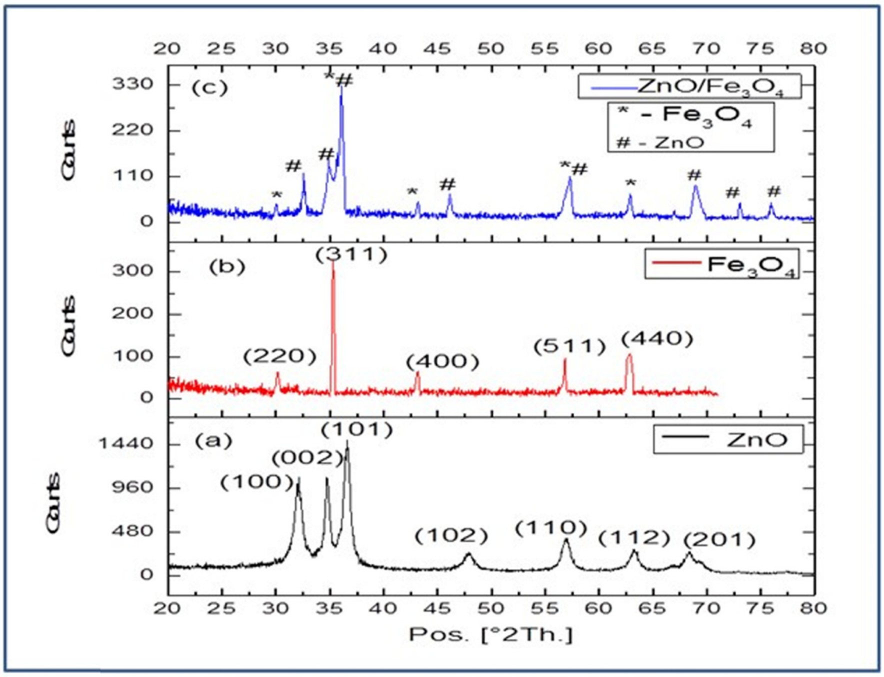

Figure 3: Powder XRD pattern of biosynthesized NPs: (a) ZnO, (b) Fe_3O_4, and (c) ZnO/Fe_3O_4 NCs.

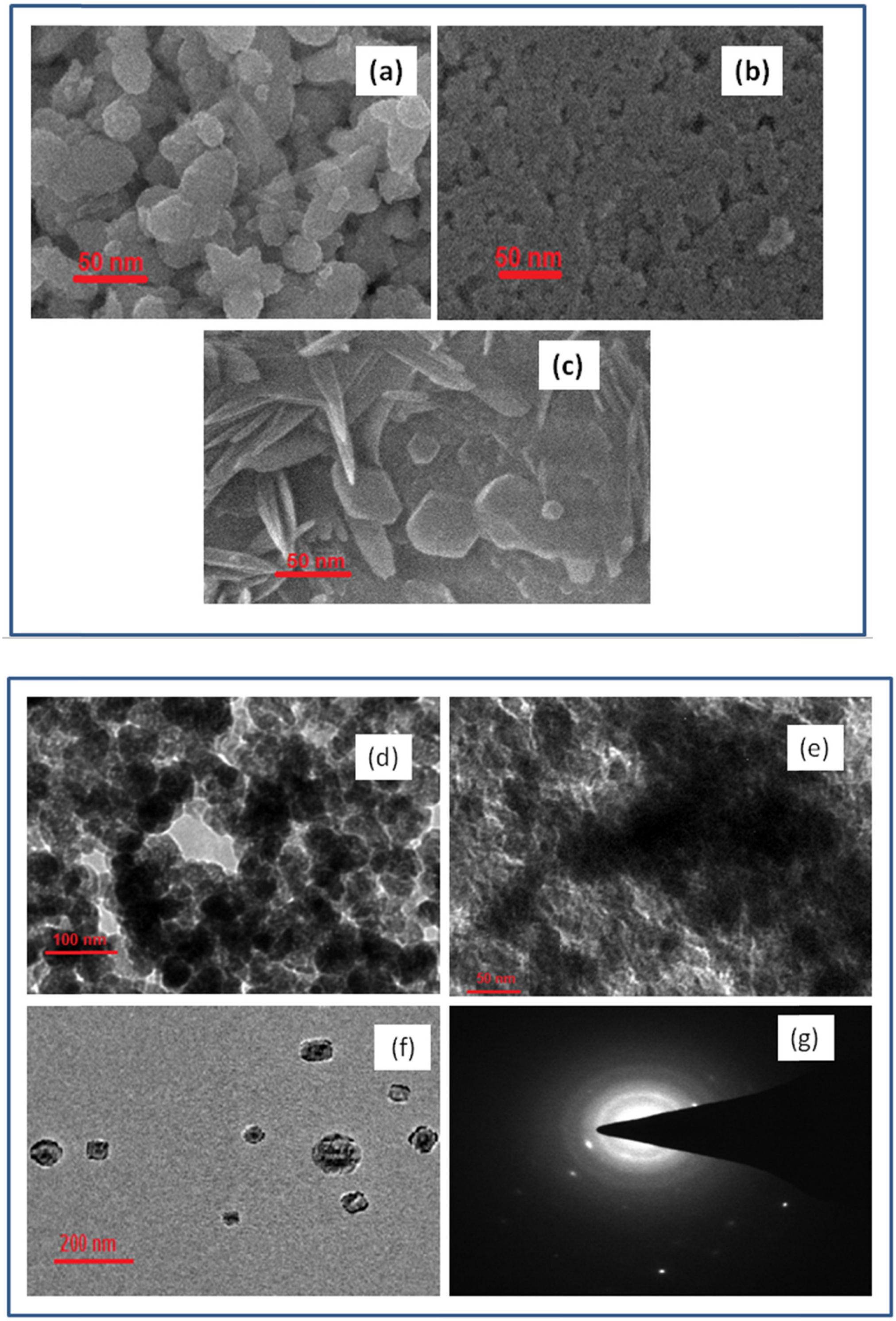

Figure 4: SEM images: (a): ZnO, (b) Fe_3O_4, and (c) ZnO/Fe_3O_4 NCs. TEM images: (d) ZnO, (e) Fe_3O_4, (f) ZnO/Fe_3O_4 NCs, and (g) SAED pattern of ZnO/Fe_3O_4 NCs.

X-ray patterns of ZnO (a), Fe_3O_4 (b), and ZnO/Fe_3O_4 (c). In Figure 3(a), XRD peaks at 2θ values = 32.03°, 34.73°, 36.66°, 48.03°, 57.05°, 68.32°, and 69.49° were indexed to the respective (100), (002), (101), (102), (110), (112), and (201) crystalline planes of hexagonal wurtzite phase of ZnO (JCPDS Card No. 36-1451), whereas in Figure 3(b), diffraction peaks at 2θ values = 30.16°, 35.29°, 43.12°, 56.83°, and 62.59° correspond to the miller indices (220), (311), (400), (511), and

(440), respectively (JCPDS Card No. 19-0629), which confirm the face-centered cubic structure of Fe_3O_4 [44]. For ZnO/Fe_3O_4 NCs (Figure 3c), peaks at 32.56°, 34.87°, 36.07°, 57.28°, 68.92°, and 69.58° corresponding to (100), (002), (101), (110), (112), and (201) planes infer the presence of ZnO in hexagonal wurtzite phase, whereas peaks at 2θ = 30.10°, 35.65°, 43.15°, and 62.86° represent (220), (311), (400), and (440) planes of face-centered cubic structure of iron. The identification of a dual phase with shifting of the respective peak values in the XRD pattern of NCs indicates the formation of Zn–Fe heterojunction. Moreover, the crystallite size (D) of as-prepared nanoproducts is calculated using Debye–Scherrer's formula ($D = k\lambda/\beta\cos\theta$) and at maximum intense peaks, the size of ZnO, Fe_3O_4, and ZnO/Fe_3O_4 is found to be 45, 35, and 60 nm, respectively.

3.3 SEM and TEM analysis

Morphology and nanoscale of the biosynthesized samples were analyzed using SEM and TEM. An overview of SEM images of Zn, Fe_3O_4, and ZnO/Fe_3O_4 samples is shown in Figure 4(a–c). As observed from images, the morphology of ZnO/Fe_3O_4 differs from ZnO or Fe_3O_4, which suggested the formation of ZnO/Fe_3O_4 NCs. Furthermore, in the SEM image of ZnO/Fe_3O_4, rod-shaped particles of ZnO and cubic-shaped structures of Fe_3O_4 are clearly visible, which interprets the interaction of Fe_3O_4 with ZnO. Morphological differences among as-prepared samples were also identified by TEM micrographs (Figure 4(d–f)). The spherical shape of ZnO NPs with a particle size of ~45 nm can be seen in Figure 4(d), whereas Fe_3O_4 NPs have an irregular shape (Figure 4(e)) with a particle size of ~35 nm. The coexistence of ZnO and Fe_3O_4 can be clearly identified in the TEM micrograph of NCs (Figure 4(f)), wherein Fe_3O_4 can identify as dark particles with some agglomeration because of its highly magnetic nature and ZnO as bright particles surrounding Fe_3O_4. Moreover, selected area electron diffraction (SAED) image of ZnO/Fe_3O_4 NCs (Figure 4(g)) also interprets the incorporation of Fe_3O_4 in the crystalline lattice of ZnO NPs, which resulted in a comparatively less crystalline and large-sized ZnO/Fe_3O_4 NCs. Thus, the results obtained from SEM and TEM analyses were in close agreement with XRD results.

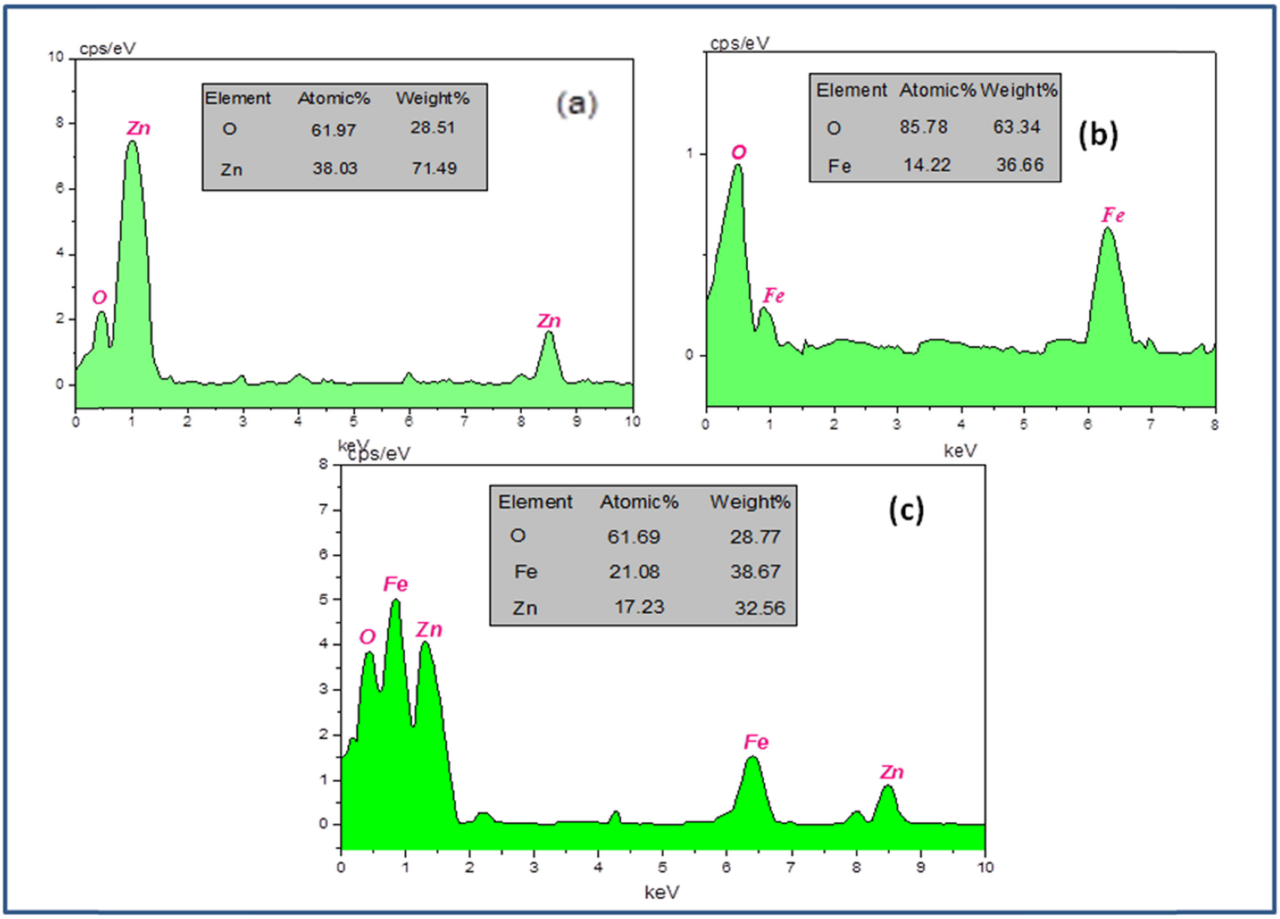

(a)

Element	Atomic%	Weight%
O	61.97	28.51
Zn	38.03	71.49

(b)

Element	Atomic%	Weight%
O	85.78	63.34
Fe	14.22	36.66

(c)

Element	Atomic%	Weight%
O	61.69	28.77
Fe	21.08	38.67
Zn	17.23	32.56

Figure 5: EDX spectrum of (a) ZnO, (b) Fe_3O_4, and (c) ZnO/Fe_3O_4 NCs.

3.4 EDX analysis

To determine the chemical composition of ZnO, Fe_3O_4, and ZnO/Fe_3O_4 nanoproducts, EDX analysis was carried out and results are displayed in Figure 5(a–c). It can be seen in Figure 5(a) that the EDX spectrum consists of strong peaks for Zn and O, whereas Figure 5(b) shows Fe and O elemental peaks. In case of ZnO/Fe_3O_4 NCs (Figure 5(c)), strong signals for Zn, Fe, and O elements were well recognized, which further confirmed the coexistence of ZnO and Fe_3O_4. The appearance of carbon in all three spectra may be due to biomolecular capping on the surface of nanoproducts [45]. Based on EDX outcomes, the weight percentage of elements in ZnO/Fe_3O_4 NCs was 32.56, 38.67, and 28.77% for Zn, Fe, and O, respectively.

3.5 XPS analysis

XPS analysis was carried out to demonstrate the chemical nature of the surface of biosynthesized ZnO/Fe_3O_4 NCs. Figure 6(a) depicts the full scan spectrum of ZnO/Fe_3O_4 and the appearance of major peaks at binding energies of 1,021 eV (Zn2p), 725 eV (Fe2p), 530 eV (O1s), and 284 eV (C1s) confirms the fabrication of ZnO/Fe_3O_4 NCs. High-resolution XPS spectra of Fe2p, Zn2p, O1s, and C1s are shown in Figure 6(b–e). In Figure 6(b), a doublet for Fe2p at 711.94 and 726.93 eV was assigned to respective binding energies of $Fe2p_{3/2}$ and $Fe2p_{1/2}$ of Fe_3O_4 [46,47]. In the Zn2p spectra (Figure 6(c)), the spin-orbit doublet $Zn2p_{3/2}$ and $Zn2p_{1/2}$ peaks were centered at binding energies of 1021.7 and 1044.65 eV, respectively [48]. It is evident from the literature that $Zn2p_{3/2}$ and $Zn2p_{1/2}$ peaks are separated by 23 eV in pure ZnO. From the XPS results, peaks of Zn2p in NCs were separated by 21 eV, which strongly manifests the synergistic effect between ZnO and Fe_3O_4 NPs, contributing to the enhancement in photocatalytic activity of NCs [49]. XPS spectrum of C1s (Figure 6(d)), consists of three peaks at 283 eV (C–C) [50], 284 eV (C═C) [46,51], and 285 eV (C═O) [52], attributed to the polyphenolic compounds of leaves' extract acting as a stabilizing agent for ZnO/Fe_3O_4 NCs [53]. In the O1s spectrum shown in

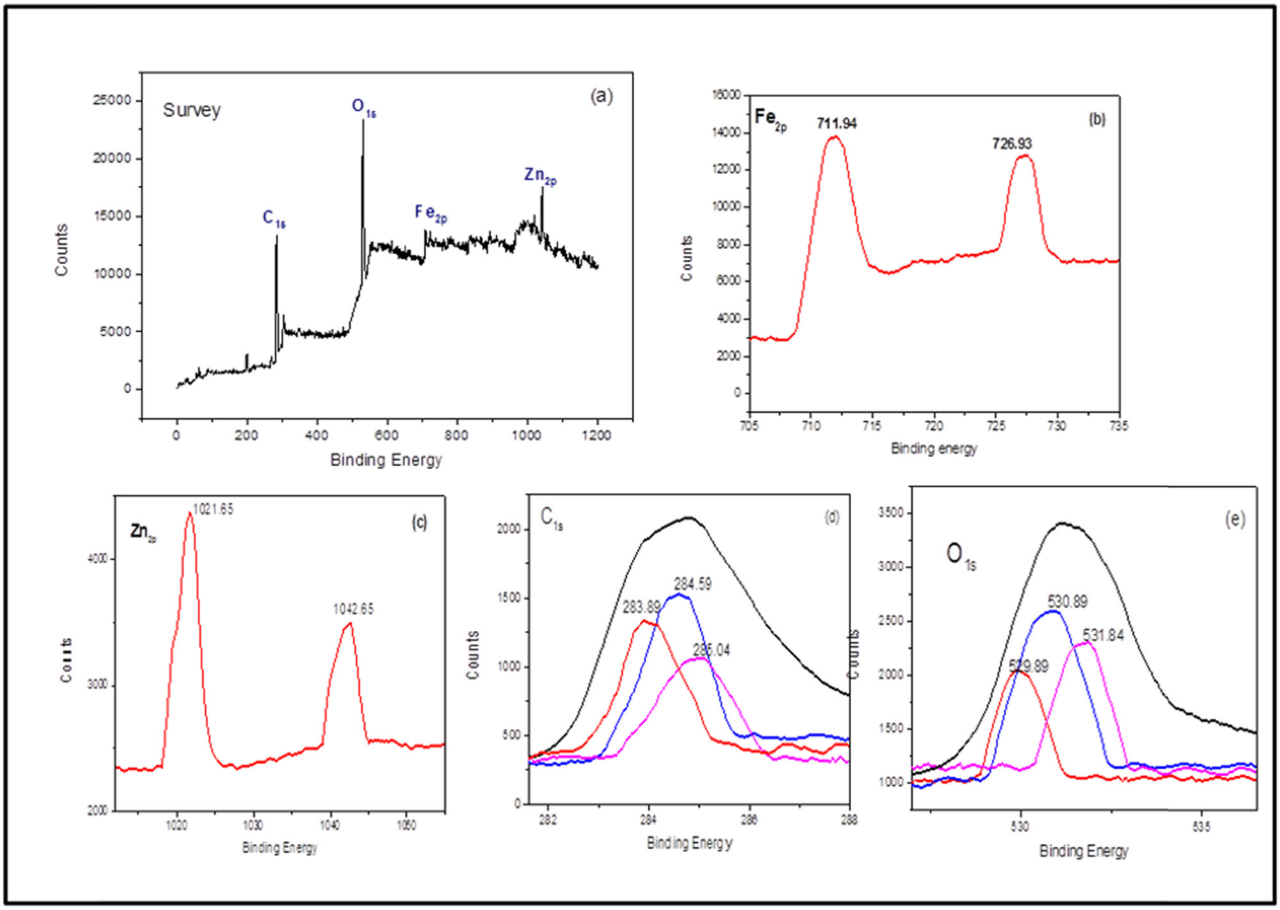

Figure 6: XPS spectra of ZnO/Fe_3O_4 NCs: (a) survey spectrum, (b) Fe2p, (c) Zn2p, (d) C1s, and (e) O1s.

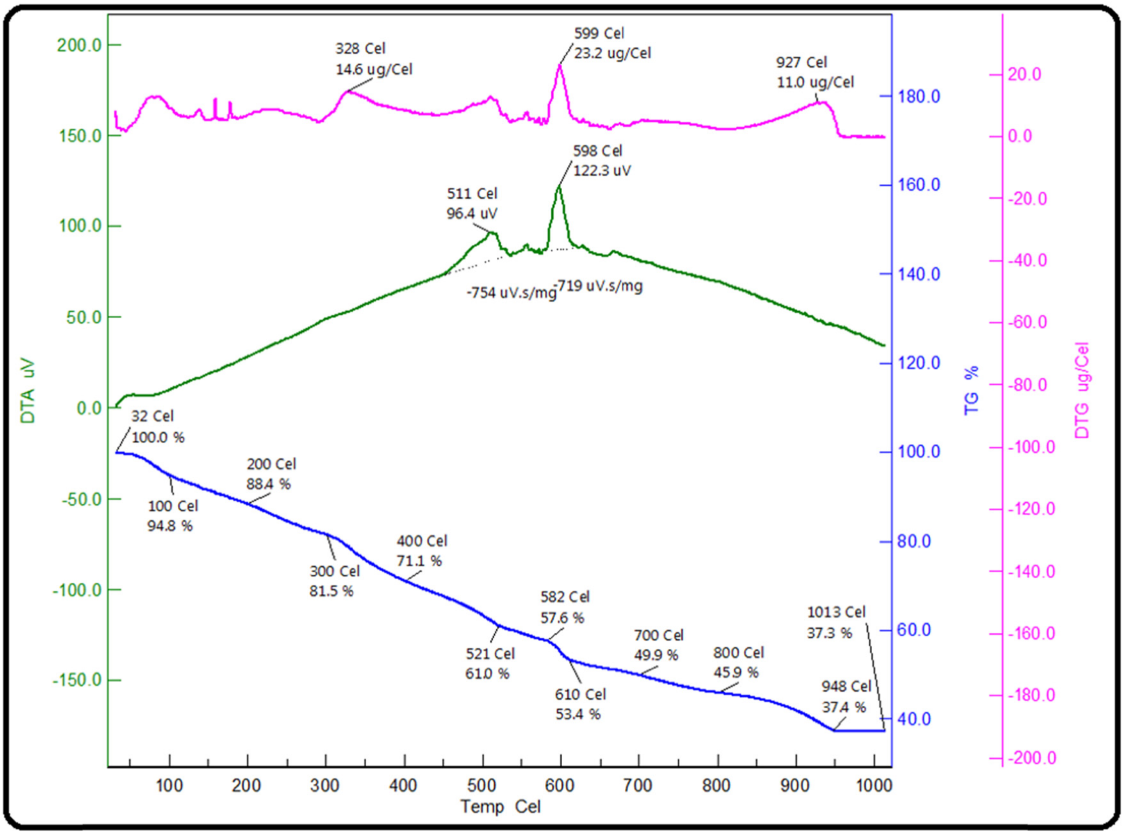

Figure 7: Thermograms of ZnO/Fe_3O_4 NCs.

Figure 6(e), the peak position at 529.89 eV was assigned to oxygen in Fe–O of ZnO/Fe_3O_4, corresponding to ferro–ferric oxide. The deconvolution of O1s signals revealed the presence of Zn–O of ZnO at a binding energy of 530.89 eV. The peak at 531.89 eV may be due to the hydroxyl group of biomolecular capping and oxygen chemisorbed onto the surface of ZnO/Fe_3O_4 NCs [54]. Under visible light irradiation, these active oxygen species on the surface of NCs may contribute to MB degradation *via* oxygen ions, such as O^{-1} and O^{-2}, which in turn improves the photocatalytic activity of ZnO/Fe_3O_4 NCs [55].

3.6 Thermal analysis

Thermal characteristics of ZnO/Fe_3O_4 NCs were determined simultaneously in a single run by using TGA and DTA (Figure 7). TGA results showed that the thermal decomposition of ZnO/Fe_3O_4 NCs occurred in four steps. Initially, up to 100°C, the weight loss of 5.2% was due to the loss of adsorbed water on the surface of NCs. The weight loss observed in the second step (200–400°C) was 17.3%, which might be due to the dismissal of biomolecules capped on the surface of NCs. The loss in weight observed in between 400 and 600°C (third step) was assigned to the adsorbed oxygen species [56]. In the last step, a loss of 7.5% in weight was observed up to 800°C. DTA thermogram (Figure 7) displayed energy changes irrespective of change in weight. The peaks observed at 328 and 599°C were associated with the release of bioactive molecules and adsorbed oxygen,

Table 1: Comparative analysis on the photoremediation of MB in the presence of biosynthesized ZnO, Fe_3O_4, and ZnO/Fe_3O_4 NCs for a period of 150 min

Sr. no.	Time (min)	ZnO (E_{max})	Fe_3O_4 (E_{max})	ZnO/Fe_3O_4 (E_{max})
1	Initially	1.32	1.32	1.32
2	15	1.239	1.29	0.956
3	30	0.987	1.19	0.854
4	45	0.914	1.12	0.806
5	60	0.865	1.023	0.772
6	75	0.722	0.992	0.578
7	90	0.682	0.93	0.485
8	150	0.202	0.829	0.012

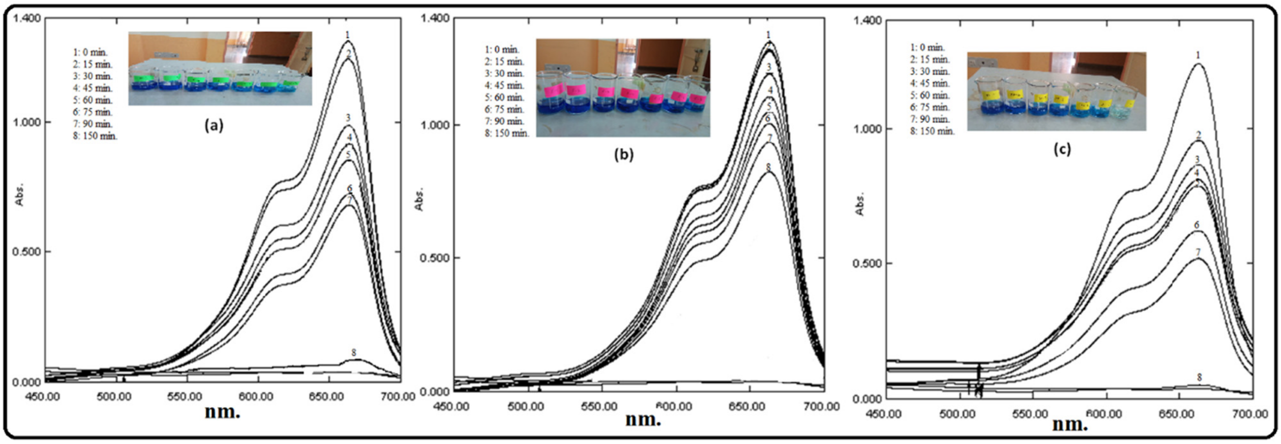

Figure 8: UV-Vis absorbance spectra of MB solution during the photocatalytic process with biosynthesized: (a) ZnO, (b) Fe_3O_4, and (c) ZnO/Fe_3O_4 NCs.

respectively. A peak at 927°C in DTA thermogram probably infers a crystalline transition of ZnO/Fe_3O_4 NCs.

3.7 Assessment of the photocatalytic activity

The photodegradation of MB in the presence of as-prepared nanoproducts was examined under visible light, and the extent of degradation was measured in terms of absorbance of MB solution using a UV-Vis spectrophotometer after certain intervals of time for 150 min. The results of degradation studies are showcased in Figures 8 and 9, and Table 1, which revealed that the degradation of MB increases with an increasing irradiation time. From the absorbance spectra of MB (Figure 8 and Table 1), it can be seen clearly that initially, 15 min of exposure to sunlight, MB solution was degraded by 6.14, 2.27, and 28.03% and after 90 min, MB solution was degraded by 48.3, 29.94, and 63.25% in the presence of biosynthesized ZnO, Fe_3O_4, and ZnO/Fe_3O_4 samples, respectively.

As shown in Figure 8, MB dye was almost completely degraded (99.09%) by ZnO/Fe_3O_4 NCs in 150 min, whereas ZnO and Fe_3O_4 NPs degraded it by 84.7 and 37.1%, respectively. These outcomes of MB absorbance spectra revealed that the degradation efficiency of ZnO NPs was increased in the presence of Fe_3O_4 NPs. The enhancement in MB removal by ZnO/Fe_3O_4 NCs compared to ZnO NPs indicated the synergistic effect between ZnO and Fe_3O_4, assigning to the degradation of MB.

Moreover, the degradation efficiency of ZnO/Fe_3O_4 NCs was examined for three consecutive runs, and the results are shown in Figure 10.

From the results, it is clear that the composites were active up to three cycles. Although in the third cycle, the degradation efficiency was decreased (90.1%). This decrement may be due to the adsorbance of some MB on the surface of photocatalyst, which perhaps blocks some active sites of NCs and can also be due to some loss of NCs during the recovery process.

The possible mechanism for the photodegradation of MB dye over biosynthesized ZnO/Fe_3O_4 NCs under visible light is shown in Figure 11.

The phenomenon of photodegradation of MB takes place when visible light is irradiated on the photocatalyst (ZnO, Fe_3O_4, or ZnO/Fe_3O_4), which leads to the generation of electron–hole pairs in conduction/valence bands (VBs) simultaneously on the surface of the photocatalyst

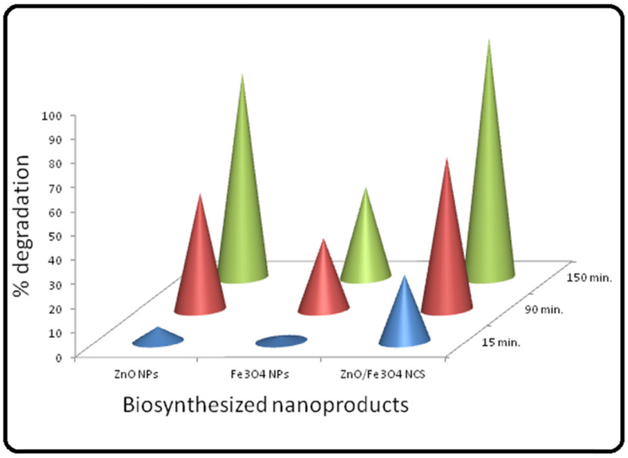

Figure 9: Graphical portrayal of percentage removal of MB at 15, 90, and 150 min in the presence of as-prepared ZnO, Fe_3O_4, and ZnO/Fe_3O_4.

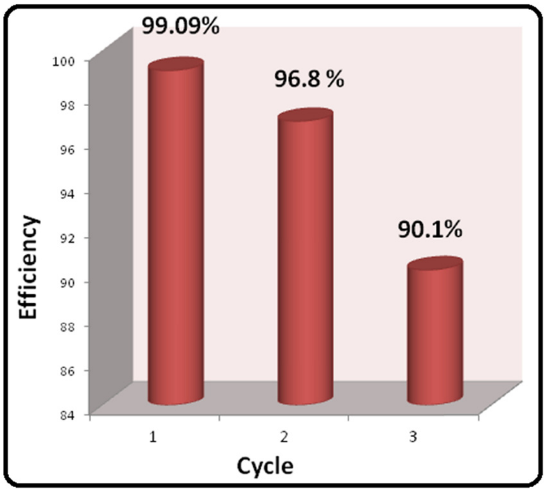

Figure 10: Reutilizing performance of ZnO/Fe_3O_4 up to three cycles.

(equation (2)). In the conduction band (CB), oxygen on the surface of the photocatalyst combines with the excited electron and forms $^{\cdot}O_2^-$ (superoxide radical; equation (3)). This radical checks the recombination of e^-/h^+ pairs by converting into $^{\cdot}OH$ radicals through hydroperoxyl radicals ($HOO^{\cdot}$) and H_2O_2 intermediates (equation (4)). Simultaneously, holes produced in VB react with the surface water to produce hydroxyl radicals ($^{\cdot}OH$; equation (5)). The hydroxyl radicals produced in CB and VB, on the surface of photocatalyst, act as a strong oxidizing agent, which in turn degrade MB molecules into simple inorganic molecules, such as water, carbon dioxide, and inorganic ions (equation (6)). The survey of the previous literature also reveals that $^{\cdot}O_2^-$ (superoxide) radicals and hydroxyl radicals ($^{\cdot}OH$) are the leading reactive species for the photodegradation of MB dye [57].

As shown in Figure 8 and Table 1, the absorption intensity of dye gradually decreases with an increasing irradiation time and finally diminished in case of ZnO/Fe_3O_4. This is because of a breakdown of the heterocyclic conjugated structure of MB molecule into simple molecules, such as water, carbon dioxide, and inorganic ions. Apart from this, the photocatalytic efficiency of ZnO/Fe_3O_4 NCs was greater compared to ZnO NPs, and this can be summarized as follows: Fe_3O_4 NPs possess a narrow bandgap, and hence, e^-/h^+ pairs produced in it under irradiation recombines fastly, as a result charge carriers could not survive for a long time for the photocatalysis process [58]. In ZnO/Fe_3O_4 NCs, the energy level of CB and VB of ZnO differs from that of Fe_3O_4. During irradiation, some photogenerated electrons from ZnO are captured by Fe_3O_4 NPs at the composite's interface, where they react with the surface oxygen to form superoxide radicals. However, some holes transfer to VB of Fe_3O_4 from ZnO and react with the surface water to produce hydroxyl radicals ($^{\cdot}OH$). This phenomenon at the interface restricts an electron–hole recombination in ZnO. As a resultant, the generation of reactive species increases at the junction of $ZnO–Fe_3O_4$, which accelerates the degradation of dye molecules [59]. Hence, the efficient charge transfer separation at heterojunction of two different semiconductor materials attributes to an enhanced photo-catalytic activity of ZnO/Fe_3O_4 NCs to degrade MB

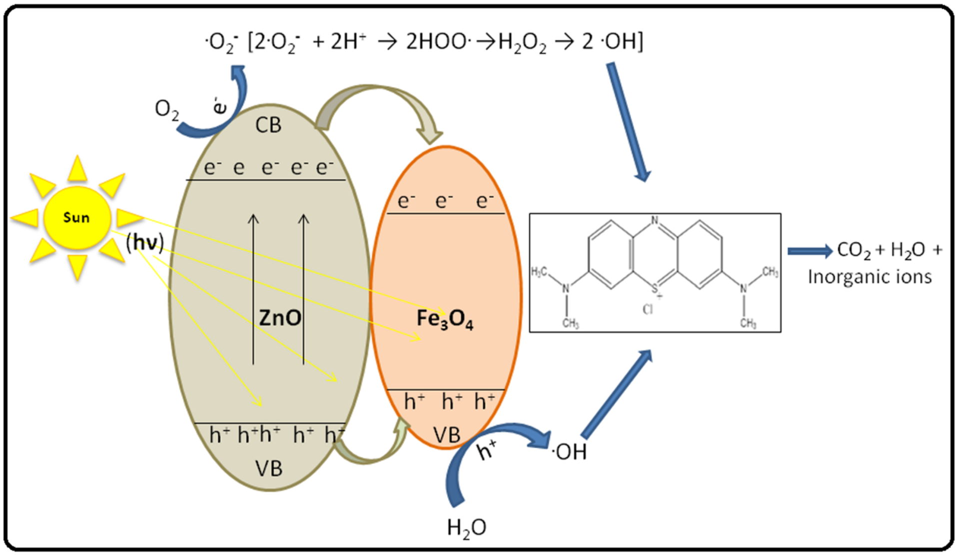

Figure 11: Possible mechanism of photocatalytic degradation of MB in the presence of *C. viminalis* leaves' extract-mediated biosynthesized ZnO/Fe_3O_4 NCs.

Table 2: A comparable study of MB dye removal by ZnO/Fe_3O_4 NCs (from the literature) with present study

S. no.	ZnO/Fe_3O_4 (ppm)	MB (ppm)	Synthesis method	Degradation time (min)	Degradation efficiency (%)	Ref.
1	50	10	Hydrothermal	180	89.2	[29]
2	500	20	One-pot synthesis	90	98.9	[37]
3	2,500	20	Microwave reactor	60	63.02	[60]
4	160	32	Biosynthesis	150	99.09	Present study

solution. However, a comparison data for photodegradation of MB dye solution by ZnO/Fe_3O_4 NCs synthesized by different routes are displayed in Table 2. The results show considerable proficiency for the current study of MB degradation by *C. viminalis*-synthesized ZnO/Fe_3O_4 NCs.

$$\text{Photocatalyst surface} + h\nu \rightarrow e^{-}_{CB} + h^{+}_{VB}, \tag{2}$$

$$2e^{-}_{CB} + 2O_2 \rightarrow 2^{\cdot}O_2, \tag{3}$$

$$\begin{aligned} 2^{\cdot}O_2^{-} + 2H^{+} &\rightarrow 2HOO^{\cdot} \rightarrow H_2O_2 \\ &\rightarrow 2^{\cdot}OH \text{ (oxidizing agent)}, \end{aligned} \tag{4}$$

$$h^{+}_{VB} + H_2O \rightarrow H^{+} + {}^{\cdot}OH \text{ (oxidizing agent)}, \tag{5}$$

$$\begin{aligned} {}^{\cdot}OH + MB \rightarrow \text{Degradation products } (CO_2 + H_2O \\ + \text{Simple inorganic ions}). \end{aligned} \tag{6}$$

4 Conclusion

In this study, ZnO/Fe_3O_4 NCs as well as ZnO and Fe_3O_4 NPs were successfully synthesized *via* eco-friendly route using *C. viminalis* leaves' extract without using any toxic additives. FTIR study indicated that the leaves' extract played a key role in the reduction and stabilization of ZnO/Fe_3O_4 NCs, ZnO NPs, and Fe_3O_4 NPs, through the interaction of O–H, C═O, and C═C groups of phytochemicals present in *C. viminalis* leaves' extract. Nanosize and the presence of pure phase in the crystal structure of biosynthesized products without major impurities, were confirmed by XRD analysis. XRD results were supported by XPS outcomes and revealed the formation of Zn–Fe heterojunction in ZnO/Fe_3O_4 NCs. Evidence of SEM, TEM, and EDX analyses also confirms the existence of Zn and Fe in composite nanoparticles. In addition, the photodegradation of MB under visible light irradiation was carried out using synthesized ZnO, Fe_3O_4, and ZnO/Fe_3O_4 as a photocatalyst. The results obtained in this study demonstrate that compared to monometallic (ZnO and Fe_3O_4) NPs, bimetallic NCs of Zn and Fe (ZnO/Fe_3O_4) accelerated the degradation of MB. The enhanced photocatalytic activity was attributed to the synergistic effect between ZnO and Fe_3O_4 nanoparticles in ZnO/Fe_3O_4 NCs. Moreover, ZnO/Fe_3O_4 NCs can be reused for three successive runs. Therefore, these findings suggest that ZnO/Fe_3O_4 NCs synthesized *via C. viminalis* leaves' extract have a potential as an efficient photocatalyst for water purification.

Acknowledgements: The authors would like to thank the Chancellor, Jaipur National University, Jaipur of India for providing laboratory facilities for this study.

Funding information: This study was funded by the Researchers Supporting Project Number (RSP-2021/339) King Saud University, Riyadh, Saudi Arabia.

Author contributions: All authors have accepted responsibility for the entire content of this manuscript and approved its submission.

Conflict of interest: The authors state no conflict of interest.

References

[1] Ajmal M, Ahmad A, Nomani AA. Physico-chemical studies on industrial pollutants. J Sci Res. 1980;2:51–3.

[2] Daneshvar N, Ayazloo M, Khataee A, Pourhassan M. Biological decolorization of dye solution containing Malachite Green by microalgae Cosmarium sp. Bioresour Technol. 2007;98(6):1176–82.

[3] He C, Yu Y, Hu X, Larbot A. Influence of silver doping on the photocatalytic activity of titania films. Appl Surf Sci. 2002;200(1–4):239–47.

[4] Nilsson I, Möller A, Mattiasson B, Rubindamayugi MS, Welander U. Decolorization of synthetic and real textile wastewater by the use of white-rot fungi. Enzyme Microb Technol. 2006;38(1–2):94–100.

[5] Mathur N, Bhatnagar P. Mutagenicity assessment of textile dyes from Sanganer (Rajasthan). J Env Biol. 2007;28(1):123–6.

[6] Hamdaoui O, Chiha M. Removal of methylene blue from aqueous solutions by wheat bran. Acta Chim Slov. 2007;54:2.

[7] López C, Valade A-G, Combourieu B, Mielgo I, Bouchon B, Lema JM. Mechanism of enzymatic degradation of the azo dye Orange II determined by *ex situ* 1H nuclear magnetic resonance

and electrospray ionization-ion trap mass spectrometry. Anal Biochem. 2004;335(1):135–49.
[8] Nagaveni K, Hegde M, Ravishankar N, Subbanna G, Madras G. Synthesis and structure of nanocrystalline TiO_2 with lower band gap showing high photocatalytic activity. Langmuir. 2004;20(7):2900–7.
[9] Aarthi T, Madras G. Photocatalytic degradation of rhodamine dyes with nano-TiO_2. Ind Eng Chem Res. 2007;46(1):7–14.
[10] Kumar SG, Rao KKJ Tungsten-based nanomaterials (WO_3 & Bi_2WO_6): modifications related to charge carrier transfer mechanisms and photocatalytic applications. Appl Surf Sci. 2015;355:939–58.
[11] Chu D, Masuda Y, Ohji T, Kato K. Formation and photocatalytic application of ZnO nanotubes using aqueous solution. Langmuir. 2010;26(4):2811–5.
[12] Singh P, Borthakur A, Mishra P, Tiwary D. Nano-materials as photocatalysts for degradation of environmental pollutants: challenges and possibilities. Amsterdam: Elsevier; 2019.
[13] Anjum M, Miandad R, Waqas M, Gehany F, Barakat MA. Remediation of wastewater using various nano-materials. Arab J Chem. 2019;12(8):4897–919.
[14] Lee KM, Lai CW, Ngai KS, Juan JC. Recent developments of zinc oxide based photocatalyst in water treatment technology: A review. Water Res. 2016;88:428–48.
[15] Wang Y, Wang Q, Zhan X, Wang F, Safdar M, He J. Visible light driven type II heterostructures and their enhanced photocatalysis properties. Nanoscale. 2013;5(18):8326–39.
[16] Kundu P, Deshpande PA, Madras G, Ravishankar N. Nanoscale ZnO/CdS heterostructures with engineered interfaces for high photocatalytic activity under solar radiation. J Mater Chem. 2011;21(12):4209–16.
[17] Kadam A, Dhabbe R, Gophane A, Sathe T, Garadkar K. Template free synthesis of ZnO/Ag_2O nanocomposites as a highly efficient visible active photocatalyst for detoxification of methyl orange. J Photochem Photobiol B. 2016;154:24–33.
[18] Pal S, Maiti S, Maiti UN, Chattopadhyay KC. Low temperature solution processed ZnO/CuO heterojunction photocatalyst for visible light induced photo-degradation of organic pollutants. CrystEng Comm. 2015;17(6):1464–76.
[19] Liu W, Wang M, Xu C, Chen S. Facile synthesis of g-C_3N_4/ZnO composite with enhanced visible light photooxidation and photoreduction properties. Chem Eng Sci. 2012;209:386–93.
[20] Thangavel S, Thangavel S, Raghavan N, Krishnamoorthy K, Venugopal G. Visible-light driven photocatalytic degradation of methylene-violet by rGO/Fe_3O_4/ZnO ternary nanohybrid structures. J Alloy Compd. 2016;665:107–12.
[21] Liu S-Q. Magnetic semiconductor nano-photocatalysts for the degradation of organic pollutants. Env Chem Lett. 2012;10(3):209–16.
[22] Mamba G, Mishra A. Advances in magnetically separable photocatalysts: smart, recyclable materials for water pollution mitigation. Catalysts. 2016;6(6):79.
[23] Boruah PK, Sharma B, Karbhal I, Shelke MV, Das M. Ammonia-modified graphene sheets decorated with magnetic Fe_3O_4 nanoparticles for the photocatalytic and photo-Fenton degradation of phenolic compounds under sunlight irradiation. J Hazard Mater. 2017;325:90–100.
[24] Mahmoudzadeh G, Khorrami S, Madani S, Frounchi M. Influence of different fuel additives at different molar ratios on the crystallite phase formation process, structural characteristics and morphology of dispersed zinc ferrite powders by sol-gel auto combustion. J Ceram Process Res. 2012;13(4):368–72.
[25] Lee H, Jung JC, Kim H, Chung Y-M, Kim TJ, Lee SJ, et al. Preparation of $ZnFe_2O_4$ catalysts by a co-precipitation method using aqueous buffer solution and their catalytic activity for oxidative dehydrogenation of *n*-butene to 1,3-butadiene. Catal Lett. 2008;122(3):281–6.
[26] Yadav RS, Havlica J, Masilko J, Tkacz J, Kuřitka I, Vilcakova J. Anneal-tuned structural, dielectric and electrical properties of $ZnFe_2O_4$ nanoparticles synthesized by starch-assisted sol–gel auto-combustion method. J Mater Sci: Mater Electron. 2016;27(6):5992–6002.
[27] Zhu H, Gu X, Zuo D, Wang Z, Wang N, Yao K. Microemulsion-based synthesis of porous zinc ferrite nanorods and its application in a room-temperature ethanol sensor. Nanotechnology. 2008;19(40):405503.
[28] Nagajyothi PC, Lee SE, An M, Duk LK. Green synthesis of silver and gold nanoparticles using Lonicera Japonica flower extract. Bull Korean Chem Soc. 2012;33(8):2609–12.
[29] Nagajyothi PC, An TNM, Sreekanth TVM, Lee J-L, Lee DJ, Lee KD. Green route biosynthesis: Characterization and catalytic activity of ZnO nanoparticles. Mater Lett. 2013;108(1):160–3.
[30] Ben AS, Sbihi HM, Azam M, Al-Resayes SI, Ayadi MT, Ayari F. Local iron ore identification: comparison to synthesized Fe_3O_4 nanoparticles obtained by ultrasonic assisted reverse co-precipitation method for Auramine O dye adsorption. Desalination Water Treat. 2021;220:446–58.
[31] Nasrollahzadeh M, Atarod M, Sajadi SM. Green synthesis of the Cu/Fe_3O_4 nanoparticles using *Morinda morindoides* leaf aqueous extract: a highly efficient magnetically separable catalyst for the reduction of organic dyes in aqueous medium at room temperature. Appl Surf Sci. 2016;364:636–44.
[32] Goyal P, Chakraborty S, Misra SKJEN. Monitoring, Management. Multifunctional Fe_3O_4-ZnO nanocomposites for environmental remediation applications. Env Nanotechnol Monit Manag. 2018;10:28–35.
[33] Nadafan M, Sabbaghan M, Sofalgar P, Anvari JZ. Comparative study of the third-order nonlinear optical properties of ZnO/Fe_3O_4 nanocomposites synthesized with or without Ionic Liquid. Opt Laser Technol. 2020;131:106435.
[34] Matinise N, Kaviyarasu K, Mongwaketsi N, Khamlich S, Kotsedi L, Mayedwa N, et al. Green synthesis of novel zinc iron oxide ($ZnFe_2O_4$) nanocomposite *via* Moringa Oleifera natural extract for electrochemical applications. Appl Surf Sci. 2018;446:66–73.
[35] Ghasemian Dazmiri M, Alinezhad H, Hossaini Z, Bekhradnia AR. Green synthesis of Fe_3O_4/ZnO magnetic core–shell nanoparticles by Petasites hybridus rhizome water extract and their application for the synthesis of pyran derivatives: Investigation of antioxidant and antimicrobial activity. Appl Organomet Chem. 2020;34(9):e5731.
[36] Cowan MM. Plant products as antimicrobial agents. Clin Microbiol Rev. 1999;12(4):564–82.
[37] Wheeler GJBS. Maintenance of a narrow host range by *Oxyops vitiosa*; a biological control agent of *Melaleuca quinquenervia*. Ecology. 2005;33(4):365–83.
[38] El-Barasi NM, Miloud MM, El-ajaily MM, Mohapatra RK, Sarangi AK, Das D, et al. Synthesis, structural investigations and antimicrobial studies of hydrazone based ternary

complexes with Cr(III), Fe(III) and La(III) ions. J Saudi Chem Soc. 2020;24(6):492–503.

[39] Taghreed HAL-N, Ranjan KM, Azam M, Leka KABK, Pranab KM, Abeer AI, et al. Mixed-ligand complexes of ampicillin derived Schiff base ligand and Nicotinamide: Synthesis, physico-chemical studies, DFT calculation, antibacterial study and molecular docking analysis. J Mol Struct. 2020;229:29832.

[40] Islam MR, Ahamed R, Rahman MO, Akbar MA, Al-Amin M, Alam KD, et al. *In vitro* antimicrobial activities of four medicinally important plants in Bangladesh. Eur J Sci Res. 2010;39(Suppl 2):199–206.

[41] Cîntă-Pînzaru S, Dehelean CA, Soica C, Culea M, Borcan F. Evaluation and differentiation of the Betulaceae birch bark species and their bioactive triterpene content using analytical FT-vibrational spectroscopy and GC-MS. Chem Cent J. 2012;6(1):1–12.

[42] Singh H, Kumar A, Thakur A, Kumar P, Nguyen V-H, Vo D-VN, et al. One-pot synthesis of magnetite-ZnO nanocomposite and its photocatalytic activity. Top Catal. 2020;63(11):1097–108.

[43] Bibi I, Nazar N, Iqbal M, Kamal S, Nawaz H, Nouren S, et al. Green and eco-friendly synthesis of cobalt-oxide nanoparticle: characterization and photo-catalytic activity. Adv Powder Technol. 2017;28(9):2035–43.

[44] Awwad AM, Salem NM. A green and facile approach for synthesis of magnetite nanoparticles. J Nanosci Nanotechnol. 2012;2(6):208–13.

[45] Karthikeyan B, Loganathan B. Rapid green synthetic protocol for novel trimetallic nanoparticles. J Nanomater. 2013;2013:2013–8.

[46] Yang T, Shen C, Li Z, Zhang H, Xiao C, Chen S, et al. Highly ordered self-assembly with large area of Fe_3O_4 nanoparticles and the magnetic properties. J Phys Chem B. 2005;109(49):23233–6.

[47] Yamashita T, Hayes P. Analysis of XPS spectra of Fe^{2+} and Fe^{3+} ions in oxide materials. Appl Surf Sci. 2008;254(8):2441–9.

[48] Haldorai Y, Voit W, Shim J-J. Nano ZnO@ reduced graphene oxide composite for high performance supercapacitor: Green synthesis in supercritical fluid. Electrochim Acta. 2014;120:65–72.

[49] Wang L, Gu H, He J, Zhao T, Zhang X, Xiao C, et al. Scale synthesized cubic $NaNbO_3$ nanoparticles with recoverable adsorption and photodegradation for prompt removal of methylene blue. J Alloy Compd. 2017;695:599–606.

[50] Cirone J, Ahmed SR, Wood PC, Chen A. Green synthesis and electrochemical study of cobalt/graphene quantum dots for efficient water splitting. J Phys Chem C. 2019;123(14):9183–91.

[51] Zhan S, Zhu D, Ma S, Yu W, Jia Y, Li Y, et al. Highly efficient removal of pathogenic bacteria with magnetic graphene composite. ACS Appl Mater Interfaces. 2015;7(7):4290–8.

[52] Sahu SK, Chakrabarty A, Bhattacharya D, Ghosh SK, Pramanik P. Single step surface modification of highly stable magnetic nanoparticles for purification of His-tag proteins. J Nanopart Res. 2011;13(6):2475–84.

[53] Akhlaghi N, Najafpour-Darzi G, Younesi H. Facile and green synthesis of cobalt oxide nanoparticles using ethanolic extract of *Trigonella foenumgraceum* (Fenugreek) leaves. Adv Powder Technol. 2020;31(8):3562–9.

[54] Wahab R, Kim Y-S, Shin H-S. Synthesis, characterization and effect of pH variation on zinc oxide nanostructures. Mater Trans. 2009;50(8):2092–7.

[55] Li J, Ng DH, Song P, Song Y, Kong C, Liu S. Synthesis of hierarchically porous Cu–Ni/C composite catalysts from tissue paper and their catalytic activity for the degradation of triphenylmethane dye in the microwave induced catalytic oxidation (MICO) process. Mater Res Bull. 2015;64:236–44.

[56] Basavegowda N, Mishra K, Lee YR. Trimetallic FeAgPt alloy as a nanocatalyst for the reduction of 4-nitroaniline and decolorization of rhodamine B: A comparative study. J Alloy Compd. 2017;701:456–64.

[57] Li N, Zhang J, Tian Y, Zhao J, Zhang J, Zuo W. Precisely controlled fabrication of magnetic 3D γ-Fe_2O_3@ ZnO core-shell photocatalyst with enhanced activity: ciprofloxacin degradation and mechanism insight. Chem Eng Sci. 2017;308:377–85.

[58] Shekofteh-Gohari M, Habibi-Yangjeh A. Fabrication of novel magnetically separable visible-light-driven photocatalysts through photosensitization of Fe_3O_4/ZnO with $CuWO_4$. J Ind Eng Chem. 2016;44:174–84.

[59] Xia J, Wang A, Liu X, Su Z. Preparation and characterization of bifunctional, Fe_3O_4/ZnO nanocomposites and their use as photocatalysts. Appl Surf Sci. 2011;257(23):9724–32.

[60] Długosz O, Szostak K, Krupiński M, Banach M. Synthesis of Fe_3O_4/ZnO nanoparticles and their application for the photodegradation of anionic and cationic dyes. Int J Env Sci Technol. 2021;18(3):561–74.